

1  
2  
3  
4  
5  
6  
7  
8  
9  
10  
11  
12  
13  
14  
15  
16  
17  
18  
19  
20  
21  
22  
23  
24  
25  
26  
27  
28  
29  
30  
31  
32  
33  
34  
35  
36  
37  
38  
39  
40  
41  
42  
43  
44

Comparison of GOES-retrieved and in-situ Measurements of Deep Convective Anvil Cloud  
Microphysical Properties During TC4

Christopher R. Yost<sup>1</sup>, Patrick Minnis<sup>2</sup>, J. Kirk Ayers<sup>1</sup>, Douglas A. Spangenberg<sup>1</sup>, Andrew J.  
Heymsfield<sup>3</sup>, Aaron Bansemer<sup>3</sup>, Matthew J. McGill<sup>4</sup>, and Dennis L. Hlavka<sup>5</sup>

<sup>1</sup>Science Systems and Applications, Inc., Hampton, VA 23666  
<sup>2</sup>NASA Langley Research Center, Hampton, VA 23681  
<sup>3</sup>National Center for Atmospheric Research, Boulder, CO  
<sup>4</sup>NASA Goddard Space Flight Center, Greenbelt, MD  
<sup>5</sup>Science Systems and Applications, Inc., Greenbelt, MD 20771

For *Journal of Geophysical Research* Special Issue on TC4

September 2009

45 Abstract

46 One of the main goals of the Tropical Composition, Cloud and Climate Coupling Experiment  
47 (TC4) during July and August 2007 was to gain a better understanding of the formation and life  
48 cycle of cirrus clouds in the upper troposphere and lower stratosphere and how their presence  
49 affects the exchange of water vapor between these layers. Additionally, it is important to  
50 compare in-situ measurements taken by aircraft instruments with products derived from satellite  
51 observations and find a meaningful way to interpret the results. In this study, cloud properties  
52 derived using radiance measurements from the Geostationary Operational Environmental  
53 Satellite (GOES) imagers are compared to similar quantities from aircraft in situ observations  
54 and are examined for meaningful relationships. A new method using dual-angle satellite  
55 measurements is used to derive the ice water content (IWC) for the top portion of deep  
56 convective clouds and anvils. The results show the in-situ and remotely sensed mean  
57 microphysical properties agree to within  $\sim 10 \mu\text{m}$  in the top few kilometers of thick anvils despite  
58 the vastly different temporal and spatial resolutions of the aircraft and satellite instruments.  
59 Mean particle size and IWC are shown to increase with decreasing altitude in the top few  
60 kilometers of the cloud. Given these relationships, it is possible to derive parameterizations for  
61 effective particle size and IWC as a function of altitude from satellite observations.

62

## 63 1. Introduction

64 Clouds play a key role in the Earth's radiation budget and hydrological cycle. The horizontal  
65 and vertical distribution of cloud water affects atmospheric and surface heating rates as well as  
66 the distribution of precipitation. Accurate determination of the 3-D cloud field for a given  
67 domain is important, not only for understanding the role of clouds in weather and climate, but  
68 also for guiding the development and refinement of cloud process models and for use in  
69 initializing forecast models (e.g., *Benjamin et al.* [2004]). Active remote sensing instruments  
70 such as lidars and radars can provide vertical profiles of cloud hydrometeor concentrations (e.g.,  
71 *Dong et al.* [2002], Wang and Sassen [2002]) and layering. Until the last few years, such  
72 information has been available only from fixed surface locations and limited aircraft  
73 measurements during field experiments. The launch of the Cloud-Aerosol Lidar and Infrared  
74 Pathfinder Satellite Observations (CALIPSO) satellite [*Winker et al.*, 2007] and CloudSat  
75 [*Stephens et al.*, 2008] have placed a cloud lidar and radar, respectively, into space producing  
76 global measurements of cloud vertical profiles. Yet, even with such advances, the active sensors  
77 still provide only cross-sections of the 3-D cloud fields at either two specific times of day  
78 (satellites) or at a single point on the Earth. Passive radiance measurements, limited as they are,  
79 remain necessary for taking measurements over all locations at all times of day. Scanning active  
80 sensors for observing clouds from a geostationary orbit are unlikely to be launched in the near  
81 future. Thus, it is important to continue researching new techniques for extracting 3-D cloud  
82 information from satellite imagers.

83 Recent advances in retrieving 3-D cloud information from passive imagery have resulted in  
84 multispectral methods for deriving profiles of cloud particle sizes (e.g., *Wang et al.* [2009]) and  
85 for detecting multi-layered clouds and retrieving their cloud properties (e.g., *Chang et al.*

86 [2009]). *Minnis et al.* [2008] used a combination of CALIPSO and Aqua Moderate Resolution  
87 Imaging Spectroradiometer (MODIS) data to improve the estimation of the physical cloud-top  
88 heights of optically thick ice clouds from infrared brightness temperature measurements, a  
89 quantity that has been subject to significant biases (e.g., *Sherwood et al.* [2004]). In the course  
90 of that analysis, *Minnis et al.*, [2008] suggested that it should be possible to retrieve ice water  
91 content (IWC) for the upper 2 km of optically thick ice clouds using passive radiance  
92 measurements from two satellite observations taken at different viewing zenith angles (VZA).  
93 The proposed method has yet to be tested. Knowing the IWC at the top of thick clouds might  
94 also be valuable for estimating the vertical distribution of IWC throughout the clouds, especially  
95 if used in conjunction with a technique like that of *Wang et al.* [2009] for profiling the effective  
96 particle sizes within the cloud.

97 The Tropical Composition, Cloud and Climate Coupling Experiment (TC4) [*Toon et al.*,  
98 2009] conducted from San Jose, Costa Rica during summer 2007 provides an opportunity for  
99 examining the new methods for inferring cloud-top IWC and validating retrievals of ice particle  
100 size and water path for deep convective clouds in the tropics during daytime. Being designed to  
101 study convectively generated cirrus clouds and transport of water vapor into the tropical  
102 tropopause layer (TTL), TC4 conducted numerous flights both within and above deep convective  
103 clouds. Cloud-top height and vertical profiles of cirrus clouds were observed with a high-altitude  
104 down-looking lidar, while in situ instruments measured particle sizes and IWC. In this paper, the  
105 dual-angle technique for retrieving IWC in the cloud tops is developed and applied to  
106 Geostationary Operational Environmental Satellite (GOES) data. The retrievals of IWC, cloud  
107 ice crystal effective size, and ice water path (IWP) are examined by comparing with the aircraft-  
108 based measurements of the same quantities. The results are discussed in light of the complexities

109 of the cloud systems and the limitations of observational consistency among the measurements.  
110 The analysis should provide a better estimate of how these new methods can resolve parts of the  
111 3-D cloud structure.

112

## 113 **2. Data**

114 The Tenth and Twelfth Geostationary Operational Environmental Satellites (GOES-10/12)  
115 provided valuable radiance measurements over the entire TC4 domain for the duration of the  
116 experiment. GOES-10 and GOES-12 are situated on the Equator at 60°W and 75°W,  
117 respectively, and have a nominal spatial resolution of 4 km at nadir. Four spectral channels are  
118 common to both satellites: visible (VIS, 0.65  $\mu\text{m}$ ), shortwave infrared (SIR, 3.9  $\mu\text{m}$ ), water vapor  
119 (WV, 6.7  $\mu\text{m}$ ), and infrared (IR, 10.8  $\mu\text{m}$ ). The fifth channels on GOES-10 and 12, respectively,  
120 are the split window (SPW, 12.0  $\mu\text{m}$ ) and CO<sub>2</sub>-slicing (COS, 13.3  $\mu\text{m}$ , 8-km resolution). GOES  
121 imagery typically had temporal resolution of 15-30 minutes over the TC4 domain.

122 The NASA DC-8 aircraft, managed during TC4 by the University of North Dakota, was  
123 equipped with an array of sensors designed to take remote and in-situ measurements of clouds,  
124 aerosols, and gases [Toon *et al*, 2009]. The aircraft is capable of flights to an altitude of 12 km  
125 for durations exceeding 10 hours and made a total of 13 science flights during TC4. The DC-8  
126 flew through both low- and high-level clouds taking measurements at different levels within  
127 clouds and occasionally obtaining profiles of various properties from cloud top to base. Of  
128 particular interest for this study are measurements of cloud particle size and frozen water  
129 content. During TC4, the DC-8 was equipped with two cloud probes, the two-dimensional  
130 cloud-imaging probe (2D-CIP) and precipitation-imaging probe (2D-PIP), designed to measure  
131 the size of cloud and precipitation particles. Combined, CIP and PIP, simply referred to

132 hereafter as CIP, have a dynamic range of 25-6400  $\mu\text{m}$  and have resolutions of 25  $\mu\text{m}$  and 100  
133  $\mu\text{m}$ , respectively [Kingsmill *et al.*, 2004].

134 The NASA ER-2 high altitude aircraft flew a total of 13 science flights during TC4 carrying  
135 a variety of remote sensors. Among these sensors was the Cloud Physics Lidar (CPL), an active  
136 remote sensor designed to take multispectral measurements of cirrus, subvisual cirrus, and  
137 aerosols with high temporal and spatial resolution [McGill *et al.*, 2002]. Measurements of  
138 backscatter from the 355-, 532-, and 1064-nm channels are used to determine the altitude and  
139 optical depth of up to 10 cloud or aerosol layers. The lidar beam is completely attenuated by  
140 features with optical depths greater than  $\sim 3$  and is unable to detect cloud and aerosol features  
141 beyond this limit. Because of its sensitivity to weakly scattering particles, high temporal and  
142 spatial resolution, and range-resolving ability, the CPL is a valuable instrument for validating  
143 cloud-top heights derived from passive satellite radiance measurements.

144

### 145 **3. Methodology**

146 Aircraft instruments often measure cloud properties that are not directly comparable to  
147 quantities derived from satellite instruments. Typically, they measure instantaneous quantities  
148 that may vary significantly in time and space while passive spaceborne sensors usually provide  
149 column-integrated quantities. In the case of optically thick anvils, satellite derived cloud  
150 properties tend to be representative of conditions near cloud top while aircraft are capable of  
151 profiling the entire cloud. In this section, we describe methods to derive quantities from aircraft  
152 and satellites observations that are more analogous to each other. This makes the comparison of  
153 aircraft- and satellite-derived cloud properties a more feasible task.

154

155 **3.1 Satellite retrievals**

156 All satellite cloud properties in this study were derived from GOES data as described by  
157 *Minnis et al.* [2009a]. During daytime, defined as solar zenith angle  $SZA < 82^\circ$ , the Visible-  
158 Infrared-Shortwave-infrared-Split-window Technique (VISST) is used to retrieve cloud  
159 properties including cloud effective temperature  $T_{eff}$ , effective cloud height  $Z_{eff}$ , cloud top height  
160  $Z_t$ , thermodynamic phase (water or ice), optical depth  $\tau$ , effective droplet radius  $r_e$ , and effective  
161 ice crystal diameter  $D_e$  [*Minnis et al.*, 2009b]. Liquid water path (LWP) and IWP are computed  
162 from the effective particle size and optical depth. During TC4, cloud properties were derived in  
163 near-real time from GOES imagery in order to help mission teams plan safe flight routes and  
164 maximize success in meeting science objectives [*Minnis et al.*, 2009a]. The data were later  
165 reprocessed using a revised set of algorithms and matched temporally and spatially to the flight  
166 tracks of the DC-8 and ER-2. Each sampling time from the CIP was matched to the nearest 4  
167 GOES pixels. Because high-altitude clouds can cause slight spatial mismatches when comparing  
168 cloud properties, a parallax correction was made when searching for the nearest satellite pixels.  
169 Cloud-top heights from the CPL were used to make this correction where they were available.  
170 Where no CPL data were available, the cloud-top height from VISST was used. On 17, 22, and  
171 31 July and 5 and 8 August, the DC-8 and ER-2 coordinated their flight paths and the two planes  
172 flew over the same locations within seconds of each other. For these coordinated DC-8 and ER-  
173 2 flights, the DC-8 flight track was first matched to the satellite pixels. Matched data from the  
174 CPL were then found by taking the mean of the properties within 4 km of the location of the DC-  
175 8 and within 2 minutes of the CIP sampling time.

176

177 **3.2 Computation of  $D_e$**

178 For spherical cloud droplets, size distributions  $n(r)$  are expressed as the number of particles  $n$   
179 having a radius between  $r$  and  $r + \Delta r$ , where  $\Delta r$  is the width of the size bin. However, ice  
180 particles are known to take a variety of shapes that are highly irregular and poorly represented by  
181 spheres in radiative transfer calculations [Yang *et al.*, 2003]. Instead, it is common to classify ice  
182 crystals by their length or maximum dimension  $L$  and the size distribution is therefore expressed  
183 as  $n(L)$ . To be consistent with the VISST cloud retrieval algorithms, we assume that all ice  
184 particles are hexagonal columns with length  $L$  and width  $D$ . Wyser and Yang [1998] determined  
185 a functional relationship between  $L$  and  $D$  for the case of hexagonal columns given by  $D =$   
186  $2.5L^{0.6}$ . The equation used to compute  $D_e$  in this study is

187

$$188 \quad D_e = \frac{\int D \times L D n(L) dL}{\int D \times L n(L) dL}, \quad (1)$$

189

190 following Minnis *et al.* [1998]. Computing  $D_e$  this way gives a quantity that is analogous to the  
191 particle size retrieved from satellite radiance measurements.

192

### 193 **3.3 Computation of IWC**

194 In-situ measurements from CIP provide estimates of IWC along the path of the airplane, and  
195 the VISST estimates IWP over an area including the flight path. These two values are not  
196 directly comparable, even if the IWP were uniform over the pixel area, since IWP is a column-  
197 integrated quantity. Only occasionally did the DC-8 make spiral descents through clouds to get a  
198 full IWC profile, which can then be integrated over the depth of the layer to obtain IWP. On the  
199 other hand, it may be possible to estimate IWC near cloud top if the proper set of satellite  
200 measurements was available. Sherwood *et al.* [2004] and Minnis *et al.* [2008] demonstrated that

201 the physical top of even optically thick ice clouds is underestimated when using a standard IR  
 202 cloud-top retrieval method. Instead, the height retrieved by IR-based methods typically lies 1-2  
 203 km below the actual physical top. Based on this difference between the physical and radiating  
 204 top of the cloud, *Minnis et al.* [2008] suggested that IWC could be retrieved from passive  
 205 radiance measurements given two satellite observations that observe a given scene from different  
 206 VZAs. IWC is defined as

$$208 \quad IWC = \frac{2\rho_i \tau D_e}{3Q_e \Delta z}, \quad (2)$$

209  
 210 where  $\rho_i = 0.9 \text{ g cm}^{-3}$  is the bulk density of ice,  $\tau$  is the optical depth of the cloud layer in the  
 211 VIS channel,  $Q_e = 2.0$  is the extinction efficiency, and  $\Delta z$  is the thickness of the cloud layer. For  
 212 two satellites viewing the same cloud, there are two retrievals of cloud effective temperature  $T_{eff1}$   
 213 and  $T_{eff2}$  from two different viewing angles  $\theta_1$  and  $\theta_2$ . If  $\theta_1 > \theta_2$ , then  $T_{eff1} < T_{eff2}$  because more of  
 214 the upper, colder portion of the cloud is along the line-of-sight of the satellite viewing at  $\theta_1$ ,  
 215 while the one viewing at  $\theta_2$  detects more IR radiance from deeper in the cloud, where the  
 216 temperature should be greater than near cloud top. Thus  $T_{eff1}$  will be observed at a higher altitude  
 217  $Z_{eff1}$ , in a local temperature sounding than  $T_{eff2}$ , observed at altitude  $Z_{eff2}$ . If it is assumed that the  
 218 difference between the heights  $\Delta Z_{eff} = Z_{eff1} - Z_{eff2}$  is due entirely to different VZAs, then it is  
 219 possible to estimate IWC in the cloud layer as represented by  $\Delta Z_{eff}$  given by

$$221 \quad IWC = \frac{2\rho_i \Delta \tau D_e}{3Q_e \Delta Z_{eff}} \quad (3)$$

222

223 where

224

$$225 \quad \Delta\tau = l(\cos \theta_2 - \cos \theta_1), \quad (4)$$

226

227 and  $l \approx 1.3$  as discussed in *Minnis et al.* [2008]. *Coakley and Davies* [1986] referred to  $l$  as the  
228 diffusion length. Substituting (4) into (3), the equation for IWC becomes

229

$$230 \quad IWC = lD_e \frac{2\rho_i}{3Q_e} \frac{\mu_2 - \mu_1}{Z_{eff1} - Z_{eff2}}, \quad (5)$$

231

232 where  $\mu_1$  and  $\mu_2$  are the cosines of  $\theta_1$  and  $\theta_2$ , respectively. It follows that if  $\mu_1 = \mu_2$  or  $Z_{eff1} =$   
233  $Z_{eff2}$ , then no IWC retrieval is possible. Furthermore, there is more confidence in the retrieval  
234 when the difference between  $\mu_1$  and  $\mu_2$  is not small. In practice, the average value of  $D_e$  from the  
235 two angles is used in Eq (5). Here, equation (5) is used to retrieve IWC from simultaneous  
236 satellite observations near cloud top along the DC-8 flight track. In the next section, this  
237 retrieval is compared to in-situ measurements taken by the CIP near cloud top.

238

## 239 **4. Results**

### 240 **4.1 31 July, 2007**

241 To provide the large-scale context, Figure 1 shows a composite GOES-10/12 visible-channel  
242 image from 1528 UTC, 31 July 2007. A large mesoscale complex developed off Costa Rica's  
243 Pacific coast and produced widespread anvil clouds. Plotted over the GOES imagery in red and  
244 cyan are the flight tracks of the DC-8 and ER-2, respectively. Between 1330-1600 UTC, the  
245 DC-8 and ER-2 flew a coordinated flight pattern among these convective cores and anvils. The

246 ER-2 flew over the system at altitudes of ~20 km allowing the CPL to observe the highest cloud  
247 tops, while the DC-8 flew directly beneath the ER-2 at altitudes below 12 km taking in-situ  
248 particle size and IWC measurements.

249 Cloud properties derived along the aircraft flight track between 1330-1600 UTC are  
250 summarized in Figure 2. Figure 2a displays the 532-nm backscatter profiles obtained by the CPL  
251 aboard the ER-2. Weak molecular scattering is shown as shades of purple while successively  
252 stronger scattering due to clouds is shown as greens, blues, reds, and white. Cloud-top altitudes  
253 are between 15-18 km throughout this segment of the flight, well above the altitude of the DC-8.  
254 Most of the clouds observed along this segment were thick enough to fully attenuate the lidar  
255 beam although optically thin cirrus often overlay the thick anvils, which topped out around 14  
256 km. Complete attenuation of the lidar beam is indicated in Figure 2a as “shadows” beneath  
257 strongly scattering features. The yellow and blue lines in Figure 2a indicate retrievals of  $Z_{eff}$  and  
258  $Z_t$ , respectively, derived by VISST from the GOES-10 imagery. Plotted in red is the altitude of  
259 the DC-8 throughout its flight. On this day, the DC-8 maintained its altitude several kilometers  
260 below the highest anvil top observed by the CPL. The VISST  $Z_{eff}$  very closely matches the  
261 altitude at which the CPL beam was completely attenuated and VISST  $Z_t$  lies 1-2 km above  $Z_{eff}$ .  
262 When the CPL beam is not completely attenuated by thick cirrus and detects both high and low  
263 cloud layers such as between 1530-1550 UTC, the VISST  $Z_{eff}$  and  $Z_t$  lie between the two cloud  
264 layers. Gaps appear in the VISST cloud heights and DC-8 altitude where the ER-2 briefly  
265 deviated from the flight path of the DC-8 and hence no spatially matched data are available.  
266 Figure 2b shows the VZAs for GOES-10 and 12. The GOES-10 VZA were always larger than  
267 the GOES-12 VZA by ~15°. The VZA never exceeds 35° for either GOES, so errors introduced  
268 by distorted or overlapping pixels due to extreme viewing angles are expected to be minimal.

269 Figure 2c shows the  $D_e$  derived from CIP, GOES-10, and GOES-12 in black, magenta, and  
270 aquamarine, respectively. The GOES retrievals generally follow the same trends, while the  $D_e$   
271 values from CIP vary widely as the plane changes altitude within the cloud. Figure 2d shows the  
272 IWC retrieved from CIP and GOES-10 and 12. A range of IWC values from  $< 0.0001 \text{ g m}^{-3}$  to  
273  $\sim 1.0 \text{ g m}^{-3}$  is obtained by both methods but values from CIP tend to be much higher, often by an  
274 order of magnitude. Although an IWC retrieval was attempted for optically thin and thick  
275 clouds, the retrieval should be more reliable for optically thick cirrus. The gray shading in  
276 Figure 2 highlights areas where a dual-satellite IWC retrieval was attempted and the cloud  
277 optical depth  $\tau_c > 8$ .

278 Figures 3a and b show scatter plots of  $D_e$  estimates from CIP and GOES-10 and GOES-12,  
279 respectively. While there is a considerable amount of scatter, the mean difference (CIP minus  
280 GOES) between the CIP and GOES estimates of  $D_e$  is less than  $20 \mu\text{m}$ . The CIP tends to retrieve  
281 larger particle sizes because the DC-8 was flying well below the cloud top and particle size has  
282 been shown to increase from cloud top to base [e.g., Wang *et al.*, 2009]. Figure 4 shows the  
283 IWC retrievals from GOES-10/12. The in-situ IWC is often an order of magnitude greater than  
284 the GOES value, probably because IWC is greater deeper in the cloud where the DC-8 was  
285 flying. Nevertheless, the CIP and GOES IWC values are fairly well correlated with a squared  
286 correlation coefficient  $R^2 = 0.41$ .

287

## 288 **4.2 5 August, 2007**

289 Figure 5 shows visible GOES imagery from 5 August, 2007 at 1558 UTC, From 1445 to  
290 1615 UTC, the ER-2 and DC-8 flew a coordinated path just south of the Gulf of Panama to  
291 obtain measurements of the properties of the anvils over that area. During this flight segment,

292 the DC-8 maintained a fairly constant altitude near 12 km which was also near the level of  
293 complete attenuation of the CPL as shown in Figure 6a. For optically thick clouds, the VISST  
294  $Z_{eff}$  closely matches the altitude at which complete beam attenuation occurs. When thin cirrus  
295 overlies another cloud layer,  $Z_{eff}$  is located between the two cloud layers. The difference  
296 between the GOES-10 and GOES-12 VZA was  $\sim 15^\circ$  (Figure 6b) and the maximum VZA is  $\sim 25^\circ$   
297 so errors due to pixel distortion should be small in this case as well. Again the in-situ and GOES  
298  $D_e$  follow similar trends with the largest particle sizes coinciding with optically thicker clouds  
299 (Figure 6c). The in-situ and remotely sensed IWC values vary in the same way but are offset in  
300 magnitude (Figure 6d). The DC-8 was typically 2-3 km below cloud-top where the cloud ice  
301 concentrations tend to be higher.

302 Scatter plots of  $D_e$  for 5 August show more correlation than the July 31 case (Figure 7). The  
303 mean differences between the CIP and GOES-10 and GOES-12  $D_e$  values are 15  $\mu\text{m}$  or less and  
304 are comparable to the previous case. The correlation is stronger here than in the previous case.  
305 For GOES-10 and GOES-12,  $R^2 = 0.12$  and  $0.19$ , respectively. A scatter plot of the in-situ and  
306 remotely sensed IWC shows that CIP again generally finds larger IWC values. The mean  
307 difference is small, but unlike the previous case, the CIP and GOES IWC retrievals are  
308 uncorrelated. The increased scatter may be due to errors in the retrieved cloud optical depth.

309

### 310 **4.3 All flight days**

311 Much of the scatter in Figures 3, 4, 7, and 8 is partially a result of comparing measurements  
312 obtained by instruments with very different spatial resolutions and sampling schemes. GOES  
313 pixels have a nominal spatial resolution of 4 km at nadir while the CIP samples an extremely  
314 narrow swath along the path of the DC-8. Furthermore, the DC-8 often flew several kilometers

315 below cloud-top and therefore potentially encountered very different cloud properties than those  
316 observed by space-based instruments. Because particle size and IWC can vary significantly on  
317 small horizontal and vertical spatial scales, finding a meaningful way to validate space-based  
318 estimates of these cloud properties with in-situ measurements is imperative and was one of the  
319 major science questions to be addressed by TC4 [Toon *et al.*, 2009].

320 Because the two different spatial resolutions of GOES and the CIP make comparison of  
321 instantaneous values of  $D_e$  and IWC difficult, a comparison of the mean properties is  
322 appropriate. The  $D_e$  values from CIP were binned according to the difference between the cloud  
323 top altitude observed by the CPL  $Z_{topCPL}$  and the altitude of the DC-8  $Z_{DC8}$  using a 2-km bin size.  
324 The corresponding  $D_e$  values from VISST were binned in the same way. This procedure was  
325 performed for each of the flight days when there was a significant amount of coordination  
326 between the DC-8 and ER-2. Figure 9a shows the mean CIP and GOES  $D_e$  as a function of  
327  $Z_{topCPL} - Z_{DC8}$ , where the midpoint of each 2-km bin is the abscissa. CIP values are represented  
328 by circles and the mean GOES-10/12  $D_e$  are represented by squares. Surprisingly, the CIP and  
329 GOES mean  $D_e$  both increase with the DC-8 depth below cloud-top and are well correlated ( $R^2 =$   
330 0.84). When  $Z_{topCPL} - Z_{DC8} < 4$  km, the mean GOES  $D_e$  is larger than the CIP  $D_e$  while the  
331 opposite is true when  $Z_{topCPL} - Z_{DC8} > 4$  km. When the DC-8 was near cloud-top, the CIP was  
332 only sampling small particles while the satellite is sensitive to larger particles somewhat deeper  
333 in the cloud. Therefore, the mean  $D_e$  from CIP is smaller than the mean GOES  $D_e$ . At a certain  
334 depth below cloud-top, in this case  $\sim 4$  km, the DC-8 encountered larger ice particles from which  
335 the GOES satellites received no signal. Therefore, the CIP  $D_e$  is larger than the GOES  $D_e$ .  
336 Despite the fact the GOES  $D_e$  represents an integrated quantity in the top few kilometers of the  
337 cloud, it seems to give an accurate representation, to within  $\sim 10$   $\mu\text{m}$ , of the in-situ particle size.

338 The same binning procedure described above in the particle size analysis was also carried out  
339 for IWC. The CIP measurements clearly demonstrate that mean IWC increases rapidly below  
340 cloud-top (Figure 9b). The smallest difference between the mean GOES and CIP IWC is near  
341 cloud-top where the difference between the means is  $0.043 \text{ g m}^{-3}$ . Below cloud-top, IWC  
342 increases rapidly, while the satellite-retrieved IWC remains relatively constant since the GOES  
343 represents only the top few kilometers of the cloud.

344 The same analysis was performed again for all DC-8 flights using  $Z_{eff}$  as the reference  
345 altitude instead of  $Z_{topCPL}$  and the results are shown in Figure 10. Note that although the DC-8  
346 rarely flew above  $Z_{topCPL}$ , it frequently flew above  $Z_{eff}$  as indicated by the negative values. CIP  
347 mean  $D_e$  increases monotonically from 40 to  $180 \mu\text{m}$  over a depth of  $\sim 12 \text{ km}$  (Figure 10a). The  
348 smallest particles are found close to cloud top ( $Z_{eff} - Z_{DC8} = -5$ ). The GOES mean  $D_e$  are, of  
349 course, independent of the DC-8's altitude and show a less defined trend than the CIP retrievals.  
350 The best agreement between the CIP and GOES is attained when the DC-8 was near  $Z_{eff}$  itself  
351 (i.e.,  $Z_{eff} - Z_{DC8} = 0$ ) where the two mean are within one standard deviation of each other. Note  
352 that the error bars for the CIP values become larger as  $Z_{eff} - Z_{DC8}$  increases indicating that the ice  
353 crystal size distribution broadens with altitude beneath cloud top. Similarly, the GOES IWC  
354 means are closest to their CIP counterparts and within one standard deviation of each other  
355 above  $Z_{eff}$ , as expected (Figure 10b). Like  $D_e$ , IWC exhibits increasing variability below cloud-  
356 top.

357

#### 358 **4.4 Spirals**

359 The DC-8, with its array of cloud probes, has the unique ability to obtain vertical profiles of

360  $D_e$  and IWC by spiraling up or down through the entire depth of a cloud. On 24 July, the DC-8  
361 executed an upward spiral near a developing convective core which eventually merged with  
362 another storm to the west (Figure 11). Starting around 1448 UTC the ascent was fairly gradual,  
363 taking about 35 minutes to complete (Figure 11a). Retrievals of  $Z_t$ ,  $D_e$ , and IWC from GOES-10,  
364 GOES-12, and the CIP are summarized in Table 1. The CIP  $Z_t$  was located less than 1 km  
365 above that from both GOES retrievals. The CIP  $Z_t$  is taken to be the last altitude where  
366 measureable IWC was encountered and, because it is a single value, no standard deviation is  
367 given in Table 1. The  $D_e$  retrievals agree very well, ranging from 76.6 to 80.3  $\mu\text{m}$  with standard  
368 deviations less than 20  $\mu\text{m}$ . Since the CIP measures IWC, integration over cloud depth is  
369 required to obtain IWP, which can then be compared to the GOES retrievals. Integration of IWC  
370 for this case yields  $\text{IWP} = 956 \text{ g m}^{-2}$  and since it is a single value no standard deviation is given  
371 in the table. The CIP IWP is well within the range of 796-1260  $\text{g m}^{-2}$  given by the GOES-10 and  
372 GOES-12 means, respectively. The GOES scanned this area twice, once at 1445 and again at  
373 1515 UTC, while the DC-8 was making its ascent. During this time, the cloud evolved  
374 considerably and the sampled scene was highly variable (Figures 11b-d), which together explain  
375 why the GOES  $Z_t$  and IWP standard deviations are so high.

376 Another spiral was performed on 3 August through a cirrus anvil over the Gulf of Panama  
377 (Figure 12). At 1705 UTC, the DC-8 began its descent from an altitude of 12 km, corresponding  
378 to cloud-top. This spiral was completed in 19 minutes, about half the time of the previous case.  
379 As seen in Figure 12a, the spiral was conducted near the edge of the anvil where the variability  
380 in cloud properties (Figures 11b-d) were significant. GOES-10 scanned this area at 1658 and  
381 1715 UTC and GOES-12 scanned at 1645 and 1715, but most of the pixels matched to the flight  
382 track came from the 1715 UTC scans. The CIP measurements indicate that ice crystals were

383 detected down to 6 km which is taken to be cloud base. Table 2 summarizes the cloud properties  
384 obtained for this case. There is relatively good agreement between the DC-8 and GOES-derived  
385 cloud-top heights with the former falling just within one standard deviation of the satellite  
386 values. Values of  $D_e$  are also fairly close especially for GOES-12. The CIP and GOES-12 mean  
387 values differ by only 4  $\mu\text{m}$ , or 5%. The IWP values are well within one standard deviation.  
388 Again, the agreement is best between the CIP and GOES-12 with differences of  $-47 \text{ gm}^{-2}$  or 15%.  
389 These results and those in Table 1 are only two data points, but they confirm, as suggested by the  
390 other analyses in section 4.3, that the VISST retrievals of  $D_e$ ,  $Z_t$ , and IWP, and by definition,  $\tau$ ,  
391 are representative of the anvil clouds over the TC4 domain.

392

## 393 **5. Summary and Future Work**

394 Careful analysis is required when comparing in-situ and remotely sensed cloud properties  
395 because these quantities are often not directly comparable. In this study, estimates of  $D_e$  were  
396 computed from ice crystal size distributions collected by the CIP aboard the DC-8 aircraft and  
397 compared to GOES retrievals matched in space and time. A new method to estimate IWC near  
398 cloud-top with coincident satellite observations was developed and the resulting values were  
399 compared with in-situ measurements taken by CIP. Instantaneous comparisons of both  $D_e$  and  
400 IWC show significant differences although there is some correlation between the in-situ and  
401 remotely sensed properties. On average, the  $D_e$  retrievals from GOES are an accurate  
402 representation of the in-situ particle size as measured by the CIP. The two comparisons with  
403 CIP-derived IWP indicate that the GOES-retrieved ice water path is a reasonable representation  
404 of the scene. These results are consistent with other comparisons [*Mace et al.*, 2005; *Waliser et*  
405 *al.*, 2009], which show that the VISST, on average, provides accurate estimates of IWP. The

406 results are encouraging for using the new method for retrieving cloud-top IWC using dual-angle  
407 views. While the mean GOES-retrieved IWC is in agreement with its DC-8 counterpart near  
408 cloud-top, the IWC increases rapidly with decreasing height in the cloud. The results, for at least  
409 one flight, show that the IWC near cloud top is related to that deeper in the cloud. If that  
410 correlation is common, then it becomes more likely that reasonably accurate profiles of  $D_e$  and  
411 IWC below cloud-top can be estimated from passive satellite observations alone, especially if  
412 additional spectral information is available [e.g., *Wang et al.*, 2009].

413 Knowledge of the vertical profiles of particle size and IWC are important for validating,  
414 initializing, and improving cloud process and other less sophisticated weather and climate  
415 models that explicitly include cloud microphysical properties. Thus, accurate retrievals of those  
416 quantities from geostationary satellite data should be valuable for improving numerical weather  
417 analyses and forecasts. The retrievals could also be valuable for aviation safety. Areas of large  
418 concentrations of ice ( $IWC > 1 \text{ g m}^{-3}$ ) in convective cloud systems pose a threat to aviation  
419 because ingest of too much ice in a jet engine can induce engine rollback and failure [*Lawson et*  
420 *al.*, 1998; *Mason et al.*, 2006]. If techniques can be developed to detect areas of potentially high  
421 IWC, it may be possible to provide warnings to air traffic controllers so that such incidents can  
422 be avoided. A correlation between IWC at cloud top and the IWC deeper in the cloud may be  
423 the basis for such a technique. The approach developed in this paper requires two satellites, or,  
424 at least, two different viewing zenith angles to retrieve IWC near cloud top. Thus, it would be  
425 practical for application over much of North America, which is viewed by two GOES, or for any  
426 other region where the satellite images overlap within a few minutes of each other. When the  
427 new GOES-R series of imagers [*Schmit et al.*, 2005] become available later in this decade, the

428 extra channels needed to estimate the vertical profile of  $D_e$  will be available and the technique  
429 could be further refined.

430 The results presented here represent only a first step in retrieving cloud-top IWC from  
431 passive satellite data. Much additional research is required to validate and improve the technique  
432 and to define its limits. Similarly, additional validations of the retrieved values of  $D_e$  and IWP  
433 are required to establish reliable uncertainty bounds. Those validations will require extensive  
434 comparisons with data from instruments such those on CloudSat and CALIPSO and at the  
435 Atmospheric Radiation Measurement Program sites [*Ackerman and Stokes, 2003*]. Comparisons  
436 with in situ measurements in various conditions will also be necessary for complete evaluation of  
437 the retrievals. Such efforts are currently ongoing.

438

#### 439 **Acknowledgments**

440 This research was supported by the NASA Applied Sciences Program, the Department of Energy  
441 Atmospheric Radiation Measurement Program through Interagency Agreement, DE-AI02-  
442 07ER64546, and the NOAA Center for Satellite Applications and Research GOES-R Program.

443

444

445 **References**

446

447 Ackerman, T. P., and G. Stokes (2003), The Atmospheric Radiation Measurement Program,

448 *Physics Today*, 56, 38-45.

449 Benjamin, S. G., S. S. Weygandt, J. M. Brown, T. L. Smith, T. G. Smirnova, W. R. Moninger, B.

450 Schwartz, E. J. Szoke, and K. Brundage (2004), Assimilation of METAR cloud and

451 visibility observations in the RUC. *Proc. 11th ARAM Conf.*, Hyannis, MA, October 4-8,

452 CD-ROM, 9.13.

453 Chang, F.-L., P. Minnis, B. Lin, M. Khaiyer, R. Palikonda, and D. Spangenberg (2009), A

454 modified method for inferring cloud top height using GOES-12 imager 10.7- and 13.3- $\mu\text{m}$

455 data, *J. Geophys. Res.*, submitted.

456 Coakley, J. A., Jr., and R. Davies (1986), The effect of cloud sides on reflected solar radiation as

457 deduced from satellite observations, *J. Atmos. Sci.*, 43, 1025-1035.

458 Dong, X., G. G. Mace, P. Minnis, W. L. Smith, Jr., M. Poellot, R. T. Marchand, and A. D. Rapp

459 (2002), Comparison of stratus cloud properties deduced from surface, GOES, and aircraft

460 data during the March 2000 ARM cloud IOP, *J. Atmos. Sci.*, 59, 3265-3284.

461 Kingsmill, D. E. and Co-authors (2004), TRMM common microphysics products: A tool for

462 evaluating spaceborne precipitation retrieval algorithms, *J. Appl. Meteorol.*, 43, 1598-1618.

463 Lawson, R. P., L. J. Angus, and A. J. Heymsfield (1998), Cloud particle measurements in

464 thunderstorm anvils and possible weather threat to aviation, *J. Aircraft*, 35, 113-121.

465 Mace, G. G., Y. Zhang, S. Platnick, M. D. King, P. Minnis, and P. Yang (2005), Evaluation of

466 cirrus cloud properties from MODIS radiances using cloud properties derived from ground-

467 based data collected at the ARM SGP site, *J. Appl. Meteorol.*, 44, 221-240.

468 Mason, J. G., J. W. Strapp, and P. Chow (2006), The ice particle threat to engines in flight, *Proc.*  
469 *44th AIAA Aerospace Sci. Mtg. and Exhibit*, Reno, NV, 9-12 January, AIAA 2006-206, 21  
470 pp.

471 McGill, M., D. Hlavka, W. Hart, V. S. Scott, J. Spinhirne, and B. Schmid (2002), Cloud Physics  
472 Lidar: Instrument description and initial measurement results, *Appl. Opt.*, *41*, 3725-3734.

473 Minnis, P. and Co-authors (2009a), Cloud properties determined from GOES and MODIS data  
474 during TC4, *J. Geophys. Res.*, submitted.

475 Minnis, P., S. Sun-Mack, and Co-authors (2009b), Cloud property retrievals for CERES using  
476 TRMM VIRS and Terra and Aqua MODIS data, *IEEE Trans. Geosci. Remote Sens.*,  
477 submitted.

478 Minnis, P., C. R. Yost, S. Sun-Mack, and Y. Chen (2008), Estimating the physical top altitude of  
479 optically thick ice clouds from thermal infrared satellite observations using CALIPSO data,  
480 *Geophys. Res. Lett.*, *35*, L12801, doi:10.1029/2008GL033947.

481 Minnis, P., D. P. Garber, D. F. Young, R. F. Arduini, Y. Takano (1998), Parameterization of  
482 reflectance and effective emittance for satellite remote sensing of cloud properties, *J. Atmos.*  
483 *Sci.*, *55*, 3313-3339.

484 T. J. Schmit, M. M. Gunshor, W. Paul Menzel, Jun Li, Scott Bachmeier, James J. Gurka (2005),  
485 Introducing the next-generation Advanced Baseline Imager (ABI) on GOES-R, *Bull. Amer.*  
486 *Meteor. Soc.*, *8*, 1079-1096.

487 Sherwood, S. C., J.-H. Chae, P. Minnis, and M. McGill (2004), Underestimation of deep  
488 convective cloud tops by thermal imagery, *Geophys. Res. Lett.*, *31*,  
489 10.1029/2004GL019699.

490 Stephens, G.L., D. G. Vane, S. Tanelli, E. Im, S. Durden, M. Rokey, and Co-authors (2008),  
491 CloudSat mission: Performance and early science after the first year of operation, *J.*  
492 *Geophys. Res.*, doi:10.1029/2008JD009982

493 Toon, O. B. and Co-authors (2009), Planning and implementation of the Tropical Composition,  
494 Cloud Climate Coupling Experiment (TC4), *J. Geophys. Res.*, submitted.

495 Waliser, D., and Co-authors (2009), Cloud ice: A climate model challenge with signs and  
496 expectations of progress, *J. Geophys. Res.*, 114, D00A21, doi:10.1029/2008JD010015.

497 Wang, X., K. N. Liou, S. C. Ou, G. G. Mace, and M. Deng (2009), Remote sensing of cirrus  
498 vertical size profile using MODIS data, *J. Geophys. Res.*, 114, D09205,  
499 doi:10.1029/2008JD011327.

500 Wang, Z. and K. Sassen (2002), Cirrus cloud microphysical property retrieval using lidar and  
501 radar measurements. Part I: algorithm description and comparison with in situ data, *J. Appl.*  
502 *Meteorol.*, 41, 218-229.

503 Winker, D. M., W. H. Hunt, and M. J. McGill (2007), Initial performance assessment of  
504 CALIOP, *Geophys. Res. Lett.*, 34, L19803, doi:10.1029/2007GL030135.

505 Wyser, K. and P. Yang (1998), Average ice crystal size and bulk short-wave single-scattering  
506 properties of cirrus clouds, *Atmos. Res.*, 49, 315-335.

507 Yang, P., B. A. Baum, A. J. Heymsfield, Y. X. Hu, H.-L. Huang, S.-C. Tsay, and S. Ackerman  
508 (2003), Single-scattering properties of droxtals, *J. Quan. Spec. & Rad. Trans.*, 79-80, 1159-  
509 1169.

510  
511

512 **Table 1.** Satellite and in-situ cloud properties derived from the DC-8 spiral at ~1500 UTC, 24  
 513 July 2007.  
 514

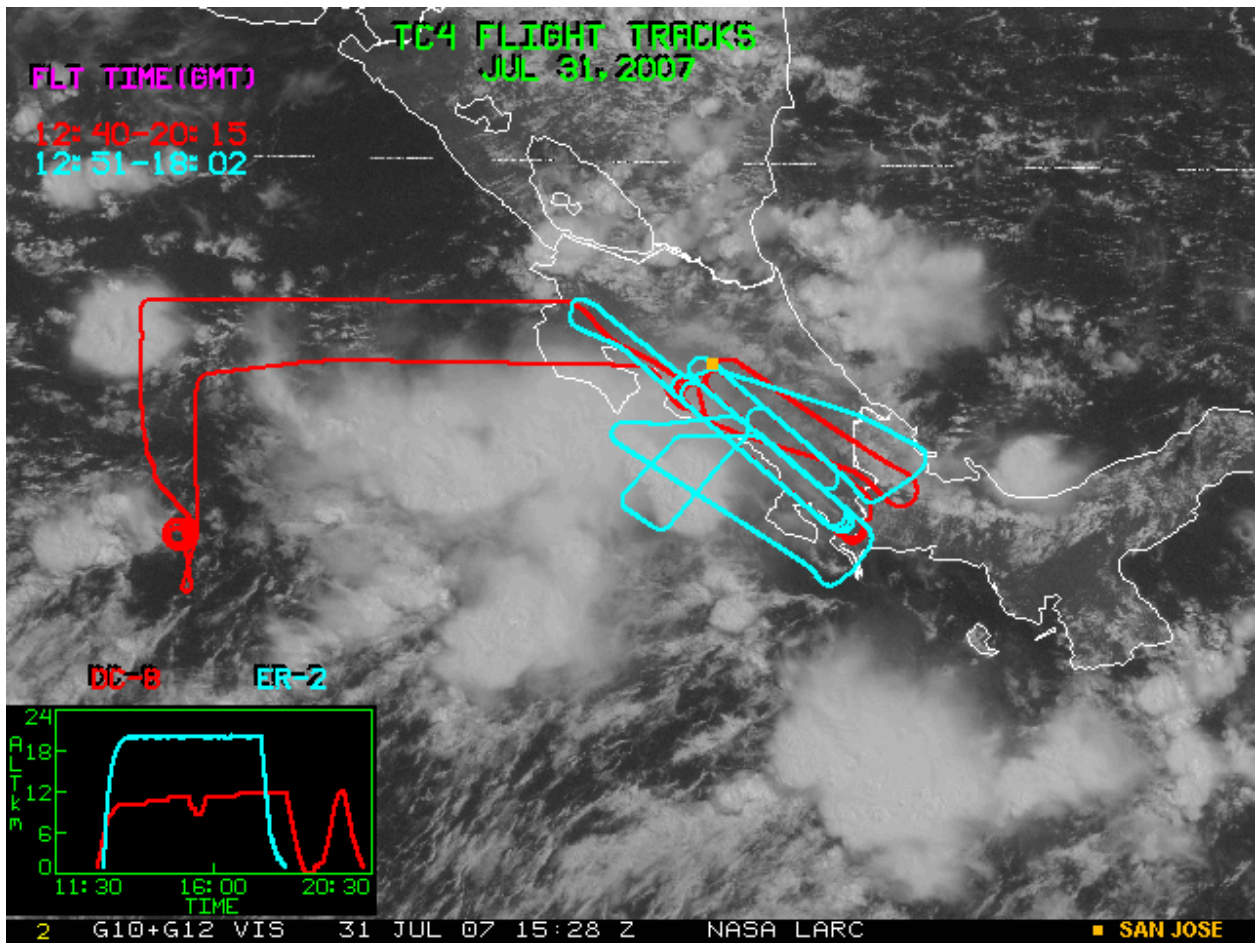
	GOES-10		GOES-12		CIP	
	Mean	SD	Mean	SD	Mean	SD
$Z_t$ (km)	11.1	3.8	10.9	4.1	11.3	-
$D_e$ ( $\mu\text{m}$ )	76.6	15.9	78.6	19.2	80.3	19.2
IWP ( $\text{g m}^{-2}$ )	795.6	795.8	1260.4	1145.6	955.6	-

515

516 **Table 2.** Satellite and in-situ cloud properties derived from the DC-8 spiral at ~1705 UTC, 3  
 517 August 2007.  
 518

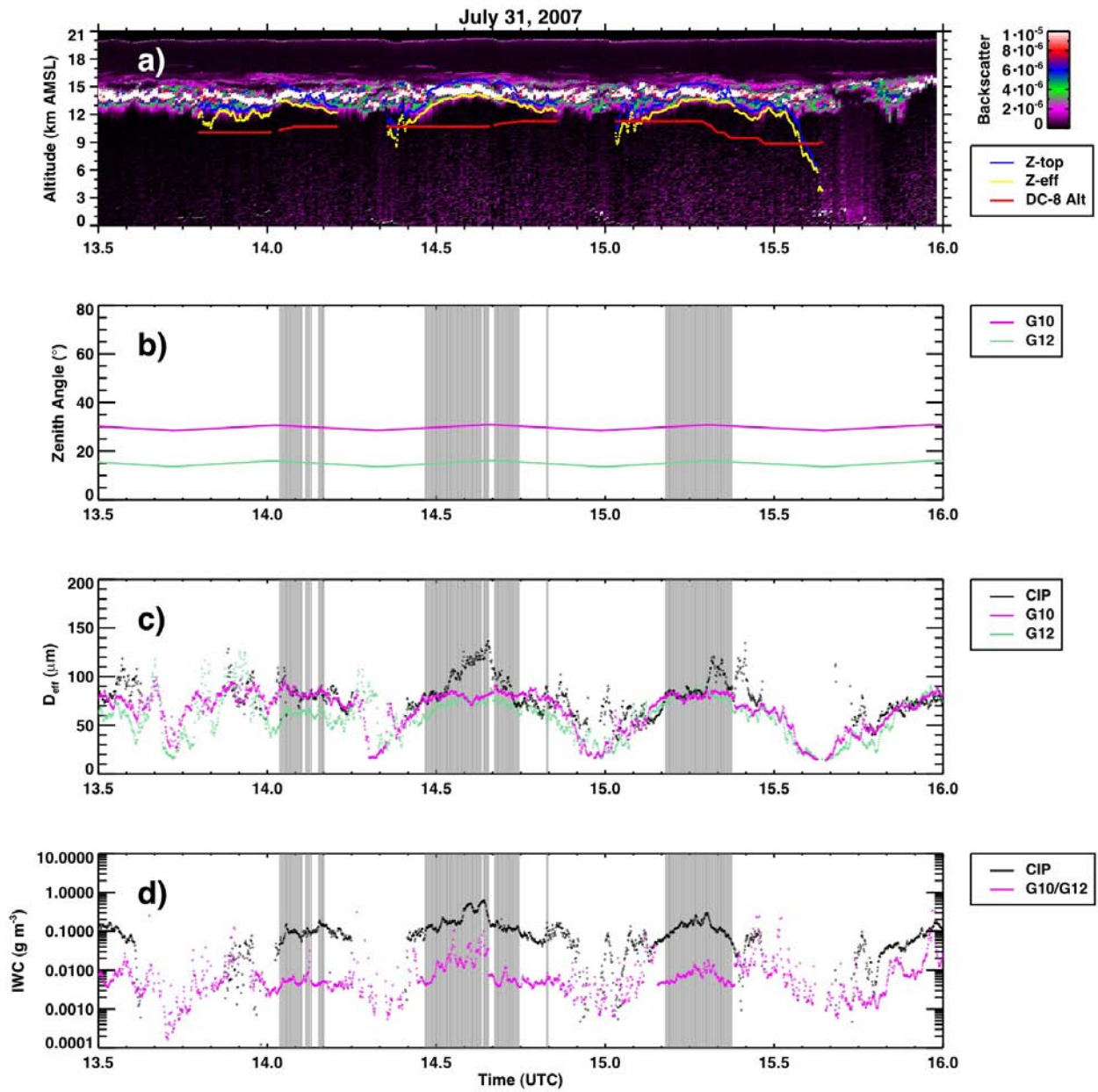
	GOES-10		GOES-12		CIP	
	Mean	SD	Mean	SD	Mean	SD
$Z_t$ (km)	12.2	0.6	12.3	0.7	11.6	-
$D_e$ ( $\mu\text{m}$ )	72.8	14.5	90.6	33.6	87.0	50.3
IWP ( $\text{g m}^{-2}$ )	185.7	102.0	276.2	188.2	322.9	-

519



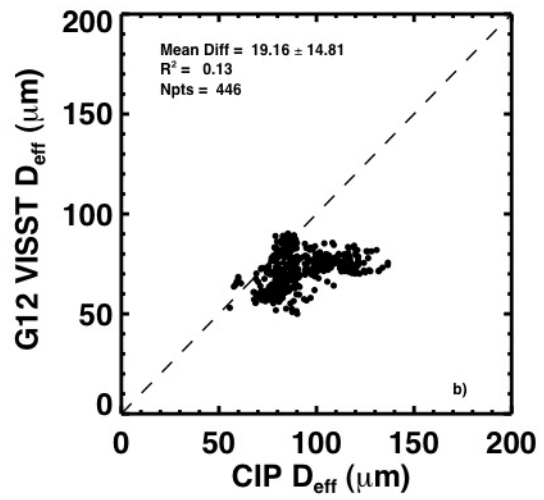
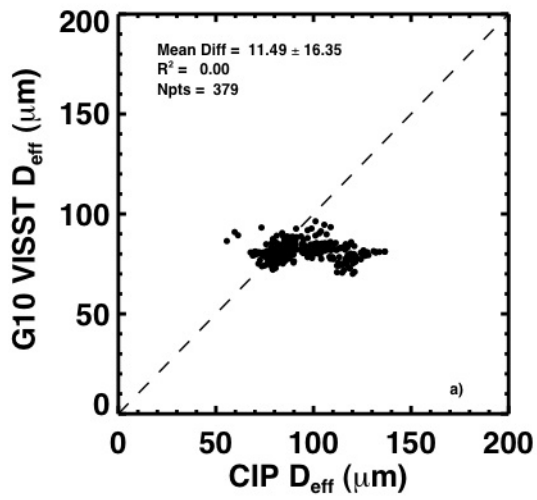
520  
521  
522  
523  
524  
525  
526  
527

**Figure 1.** Composite GOES-10/GOES-12 visible image over the TC4 domain at 1528 UTC, 31 July 2007. The flight tracks of the DC-8 and ER-2 are plotted over the image. Time series of the planes' altitudes are shown in the lower left inset.



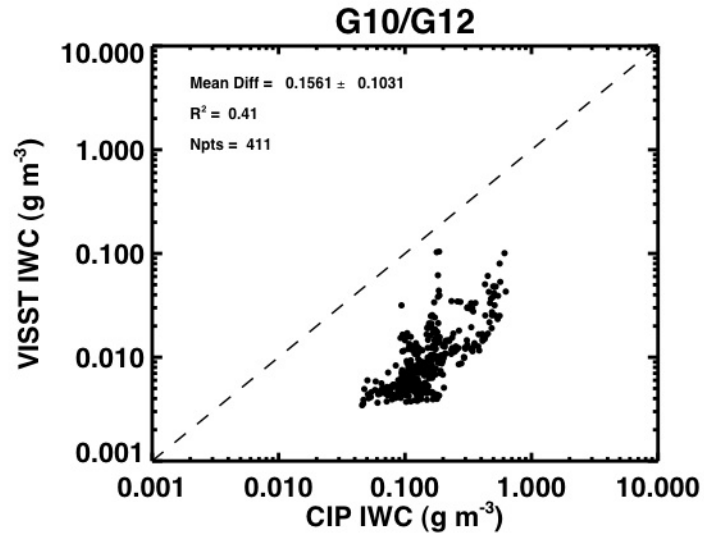
528  
 529  
 530  
 531  
 532  
 533  
 534  
 535

**Figure 2.** Time series of (a) cloud-top, effective radiating, and aircraft altitude plotted over CPL 532-nm backscatter profiles, (b) satellite VZA, (c) effective ice crystal diameter, and (d) ice water content for 31 July 2007.



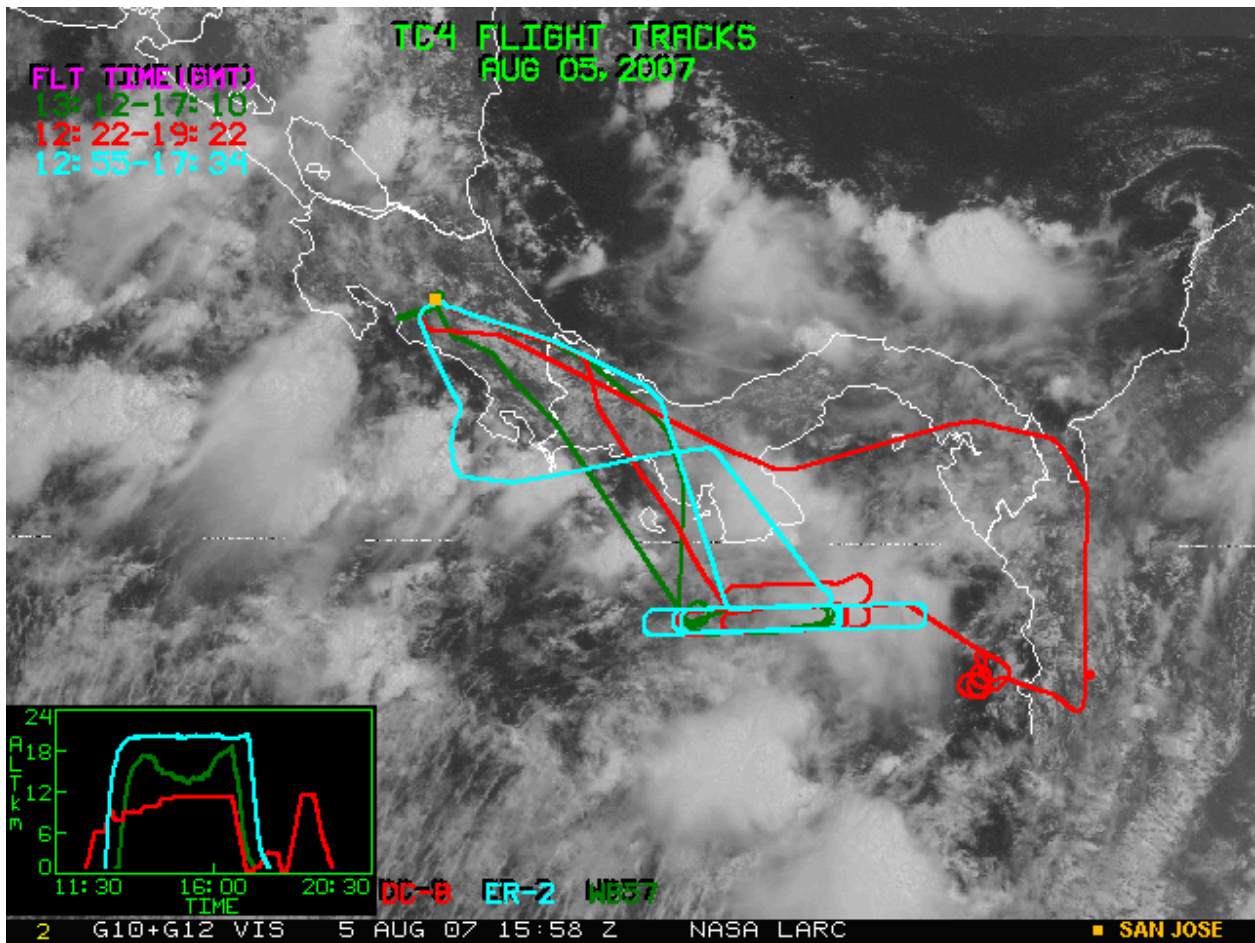
536  
 537  
 538  
 539  
 540  
 541

**Figure 3.** Scatter plots of  $D_e$  estimated from CIP and (a) GOES-10 and (b) GOES-12 for 31 July 2007.



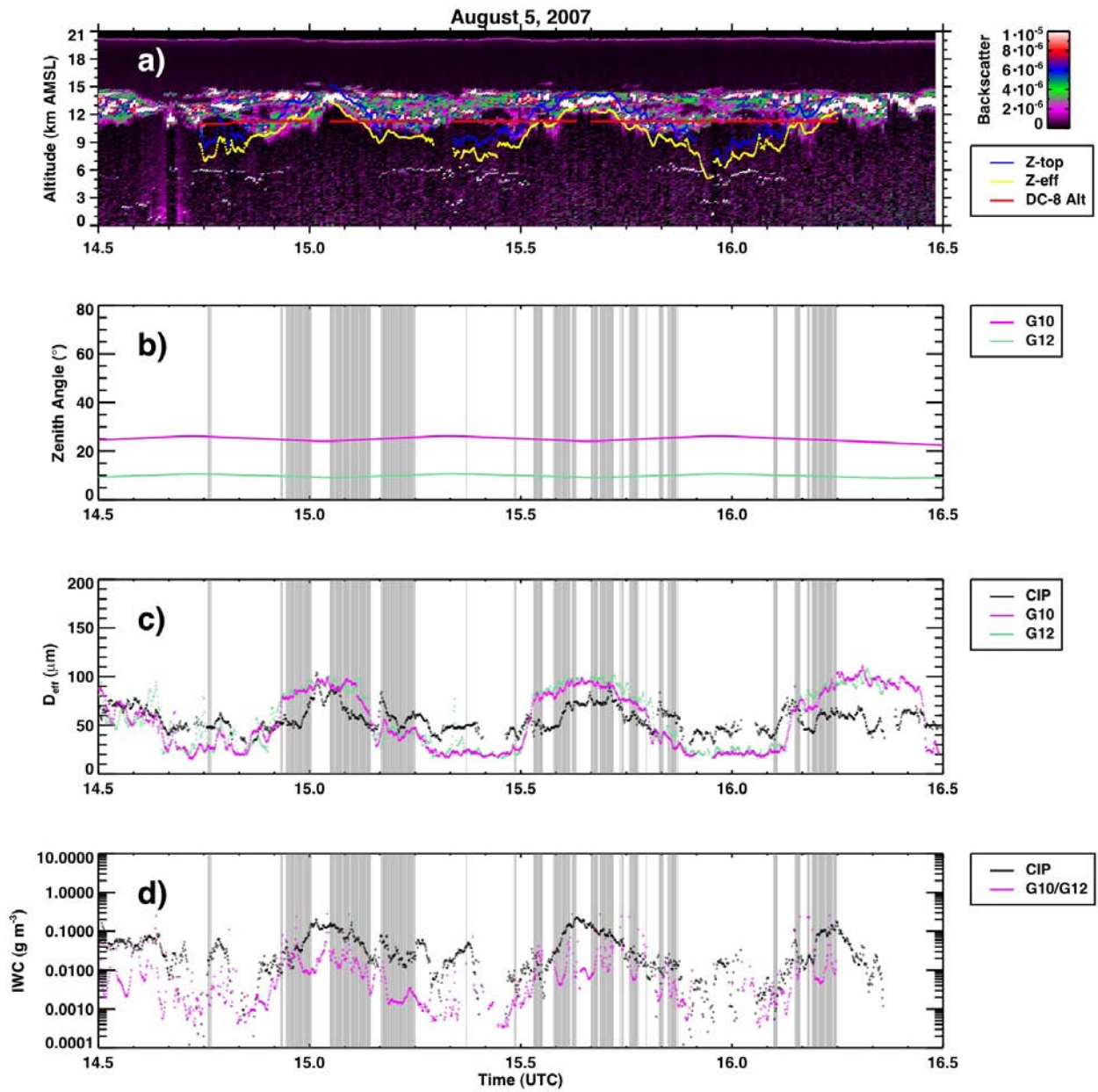
542  
543  
544  
545

**Figure 4.** Scatter plot of IWC estimated from CIP and a combination of GOES-10/GOES-12 data for 31 July 2007.

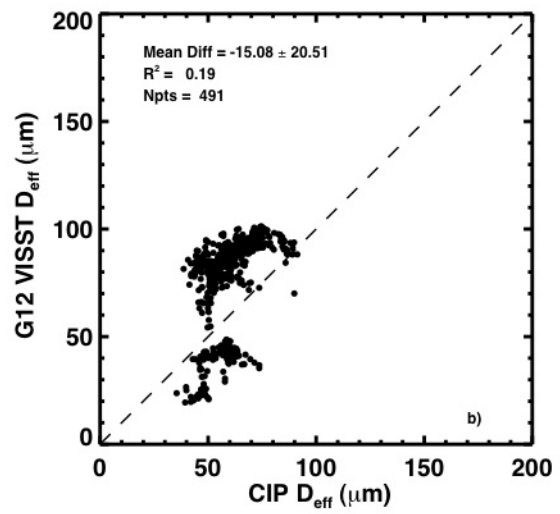
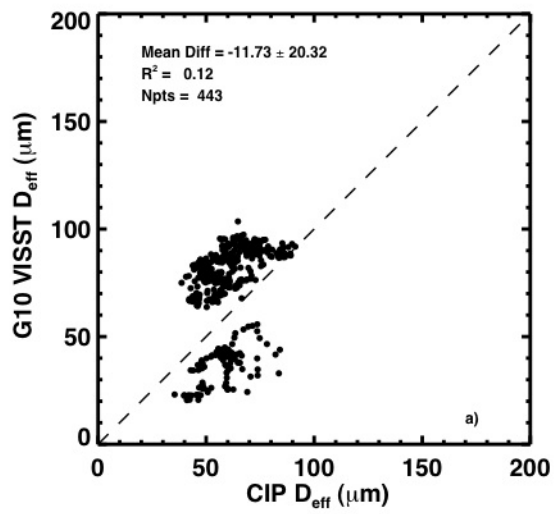


546  
547  
548  
549  
550  
551

**Figure 5.** Composite GOES-10/GOES-12 visible image over the TC4 domain at 1558 UTC, 5 August 2007. The flight tracks of the DC-8 and ER-2 are plotted over the image. Time series of the planes' altitudes are shown in the lower left inset.

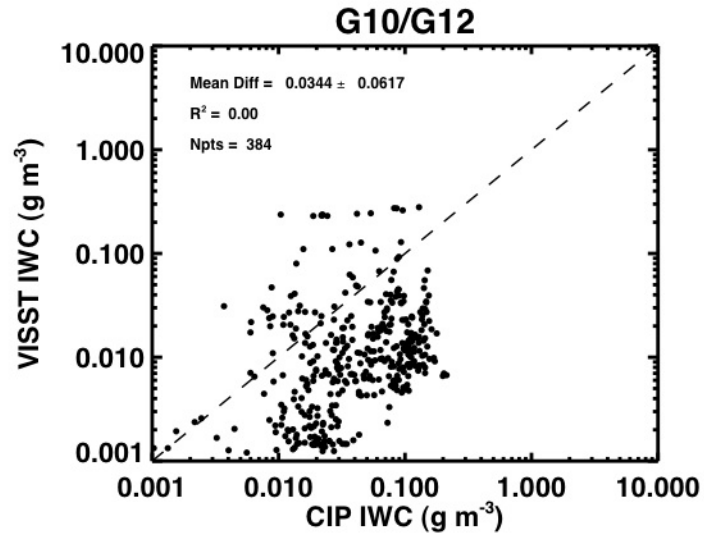


552  
 553 **Figure 6.** Time series of (a) cloud-top, effective radiating, and aircraft altitude plotted over CPL  
 554 532-nm backscatter profiles, (b) satellite VZA, (c) effective ice crystal diameter, and (d) ice  
 555 water content for 5 August 2007.  
 556



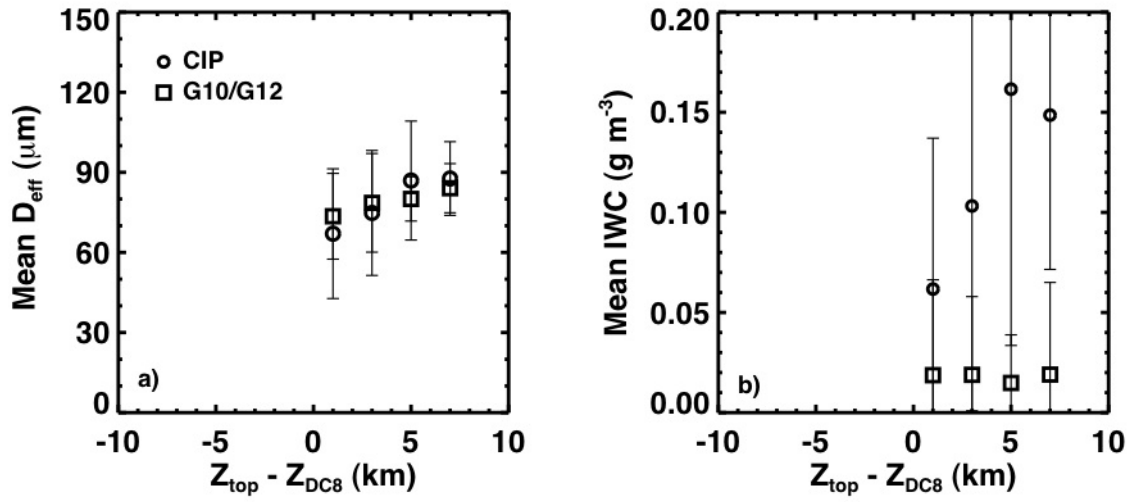
557  
 558  
 559  
 560

**Figure 7.** Scatter plots of  $D_e$  estimated from CIP and GOES-10 (a), GOES-12 (b) for August 5, 2007.



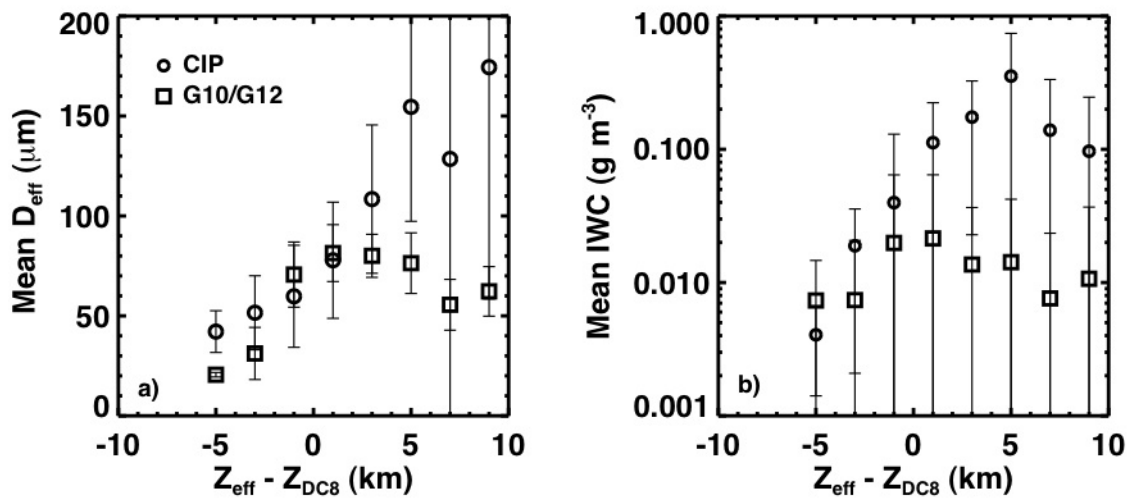
561  
562  
563  
564

**Figure 8.** Scatter plot of IWC estimated from CIP and a combination of GOES-10/GOES-12 data for 5 August 2007.



566  
 567  
 568  
 569

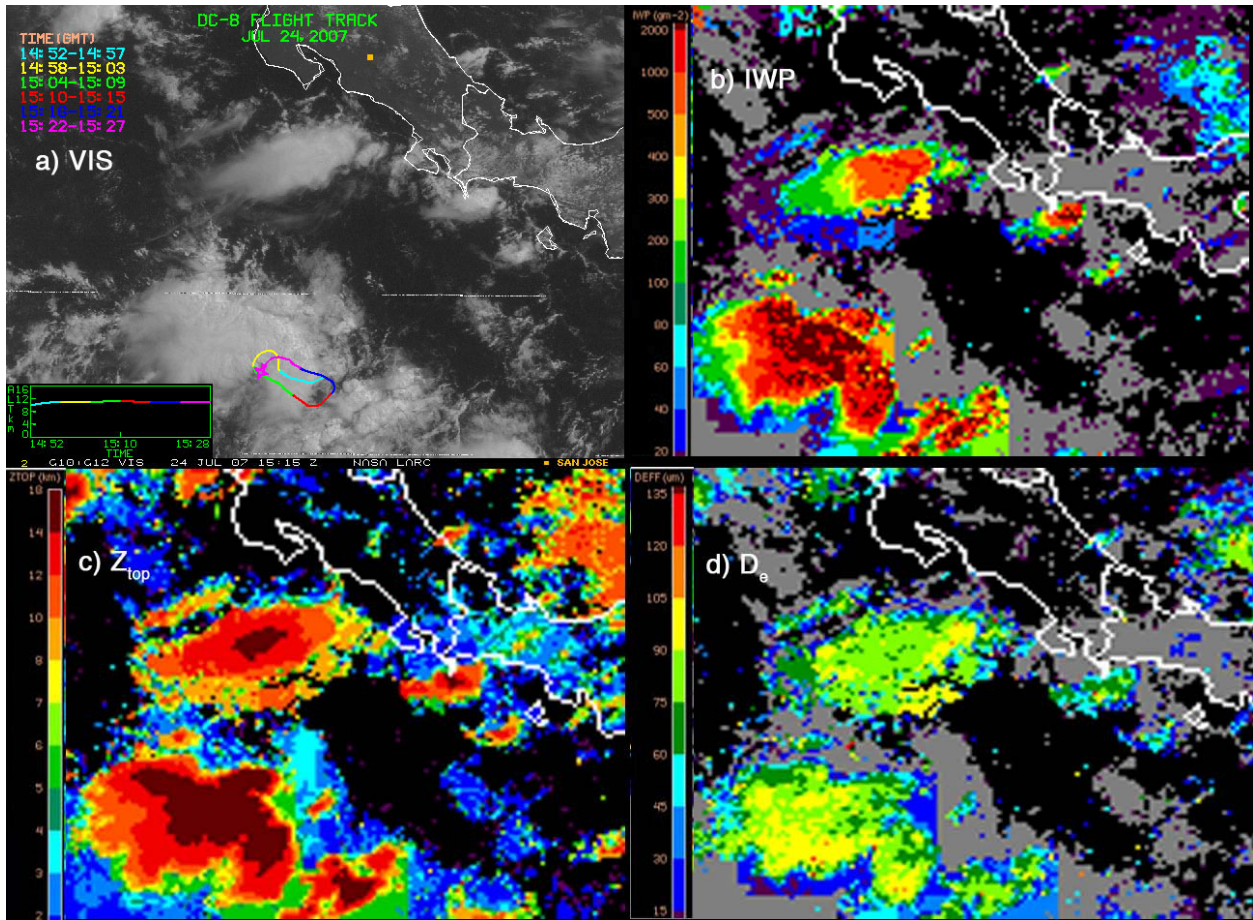
**Figure 9.** Mean (a)  $D_e$  and (a) IWC as a function of the vertical position of the DC-8 relative to the CPL  $Z_t$  for all coordinated flights with the DC-8 and ER-2.



570  
 571  
 572  
 573  
 574

**Figure 10.** Mean (a)  $D_e$  and (b) IWC as a function of the vertical position of the DC-8 relative to  $Z_{eff}$  for all DC-8 flights. The bars indicate the standard deviations of the measurements.

575



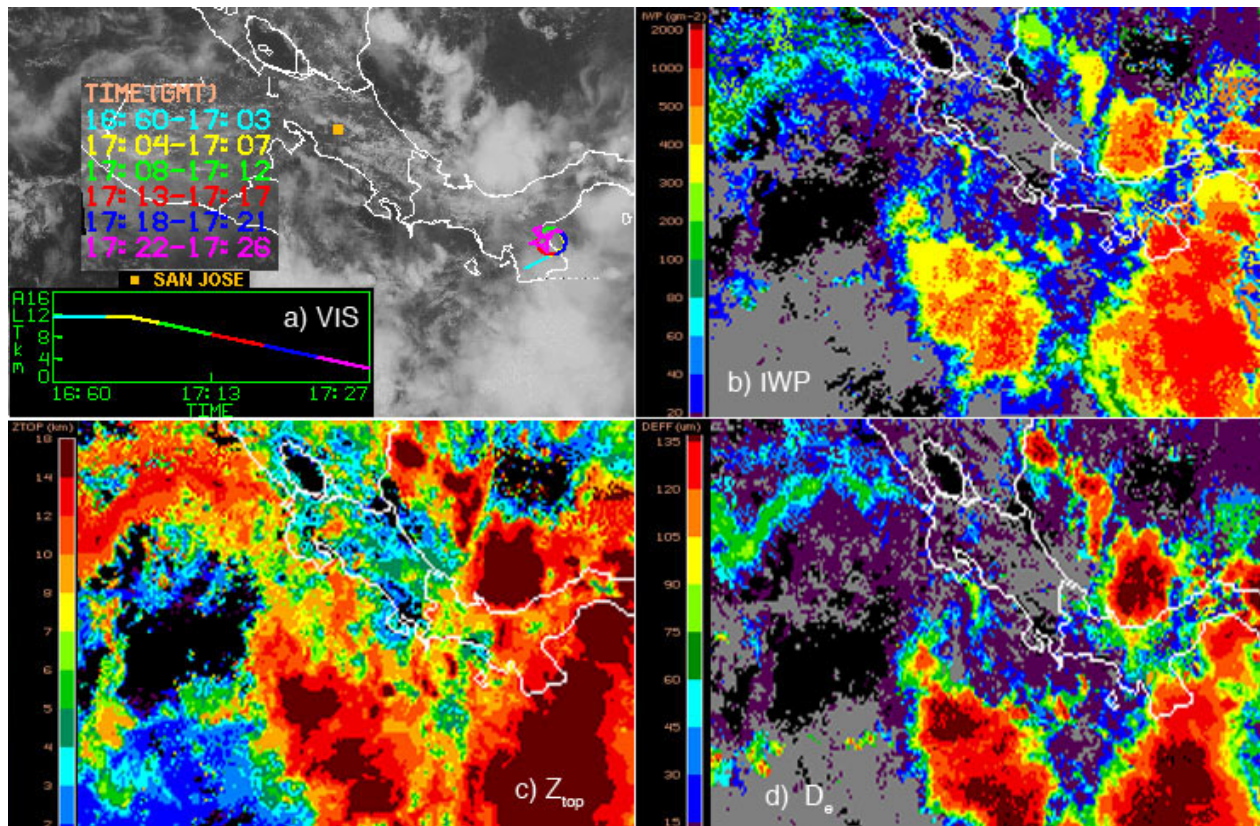
576

577

578 Figure 11. GOES-12 imagery and VISST cloud products for 1515 UTC, 24 July 2007. (a) VIS  
579 channel image with DC-8 flight track overlay; (b) IWP ( $\text{gm}^{-2}$ ), grey areas indicate water clouds;  
580 (c) Cloud-top height (km); and (d)  $D_e$  ( $\mu\text{m}$ ).

581

582



583  
584  
585  
586

Figure 12. Same as Figure 11, except for 1715 UTC, 3 August 2007.